INSTITUTE OF PHYSICS PUBLISHING WAVES IN RANDOM MEDIA

Waves Random Media **14** (2004) 365–388 PII: S0959-7174(04)68348-0

Coherent backscattering of light by complex random media of spherical scatterers: numerical solution

Karri Muinonen

Observatory, PO Box 14, FI-00014 University of Helsinki, Finland

E-mail: Karri.Muinonen@Helsinki.Fi

Received 1 September 2003
Published 24 May 2004
Online at stacks.iop.org/WRM/14/365
DOI: 10.1088/0959-7174/14/3/010

Abstract

Novel Monte Carlo techniques are described for the computation of reflection coefficient matrices for multiple scattering of light in plane-parallel random media of spherical scatterers. The present multiple scattering theory is composed of coherent backscattering and radiative transfer. In the radiative transfer part, the Stokes parameters of light escaping from the medium are updated at each scattering process in predefined angles of emergence. The scattering directions at each process are randomized using probability densities for the polar and azimuthal scattering angles: the former angle is generated using the single-scattering phase function, whereafter the latter follows from Kepler's equation. For spherical scatterers in the Rayleigh regime, randomization proceeds semi-analytically whereas, beyond that regime, cubic spline presentation of the scattering matrix is used for numerical computations. In the coherent backscattering part, the reciprocity of electromagnetic waves in the backscattering direction allows the renormalization of the reversely propagating waves, whereafter the scattering characteristics are computed in other directions. High orders of scattering ($\sim$10 000) can be treated because of the peculiar polarization characteristics of the reverse wave: after a number of scatterings, the polarization state of the reverse wave becomes independent of that of the incident wave, that is, it becomes fully dictated by the scatterings at the end of the reverse path. The coherent backscattering part depends on the single-scattering albedo in a non-monotonous way, the most pronounced signatures showing up for absorbing scatterers. The numerical results compare favourably to the literature results for nonabsorbing spherical scatterers both in and beyond the Rayleigh regime.

1. Introduction

Natural complex media of scatterers give rise to nonlinear phenomena in the angular dependences of intensity and polarization, when the illumination and observation geometries

are varied. Close to astronomical opposition, atmosphereless planetary-system objects show an opposition effect, a nonlinear increase of brightness at small solar phase angles $\alpha \leqslant 7^\circ$, the angle between the Sun and the observer as seen from the object. They show a negative polarization surge in the degree of linear polarization $(|a_\perp|^2 - |a_\parallel|^2)/(|a_\perp|^2 + |a_\parallel|^2)$ for unpolarized incident sunlight: at phase angles $\alpha \leqslant 30^\circ$, the brightness component $|a_\parallel|^2$ with the electric vector parallel to the scattering plane defined by the Sun, the object and the observer predominates over the perpendicular component $|a_\perp|^2$.

The coherent backscattering mechanism has been invoked to explain the opposition effect of planetary-system objects [1–5], as well as their peculiar negative polarization characteristics [2, 3, 6, 7]. The surfaces of the objects are likely to be composed of inhomogeneous small particles, constituting closely packed random media with random rough surfaces. A novel numerical technique is here developed for coherent backscattering by semi-infinite and finite plane-parallel media of spherical scatterers, aiming towards the interpretation of the photometric and polarimetric observations of planetary-system objects.

Lyot [8] discovered the negative polarization surge for the Moon and Saturn's rings, whereas Seeliger [9] deduced the opposition brightening of Saturn's rings from the observations of the entire Saturnian system by Müller [10]. The observations and theoretical interpretations of the photometric and polarimetric backscattering surges have been reviewed in, e.g., [11–16].

Kuga and Ishimaru [17] measured the coherent backscattering peak experimentally for dense suspensions of spherical latex particles. Simultaneously, coherent backscattering was detected by van Albada and Lagendijk [18] and Wolf and Maret [19] as a manifestation of weak localization of photons in disordered media of scatterers. Theoretically, the constructive interference in multiple scattering was already known in studies of multiple scattering of electromagnetic waves in underdense plasmas [20] and in electromagnetic scattering by extended dielectric turbulent media [21]. The spatial anisotropy of the coherent backscattering peak was experimentally documented in [22] although earlier measured by Lyot for porous media of small MgO particles [8].

Within a multiple scattering approximation consisting of the so-called ladder (or radiative transfer) and maximally crossed (or coherent backscattering) terms of the multiple scattering theory, the scattering problem has been solved exactly for plane-parallel random media composed of non-absorbing Rayleigh scatterers [23, 24]. The solution has allowed the derivation of reference enhancement factors and polarization surge depths [25]. Coherent backscattering has been studied for simplified scattering systems using both exact and approximate treatments of the electromagnetic theory. Such studies include coherent backscattering by two dipole scatterers [2, 3, 26], two spherical scatterers [27, 28], and coherent backscattering by a dipole scatterer and a semi-infinite optically homogeneous and isotropic medium [3, 30, 31]. Recently, coherent backscattering effects have been searched for spherical media of Rayleigh scatterers using the volume integral equation technique [32] and for isolated, randomly oriented tetrahedral crystals using the physical optics approximation [33].

Numerical Monte Carlo (MC) analyses of coherent backscattering by random media have been put forward by several authors [34–37]—such techniques are attractive because of their conceptual clarity and applicability to complicated non-plane-parallel geometries of the media. The present MC technique is the first one based on Stokes parameters, Mueller scattering matrices and a Jones amplitude scattering matrix formulation of the reciprocity principle for electromagnetic scattering [38–40]. Asymptotically, the technique offers an exact treatment of the approximate multiple scattering theory cited above. The reciprocity principle has earlier been used in the computation of enhancement factors in the backscattering

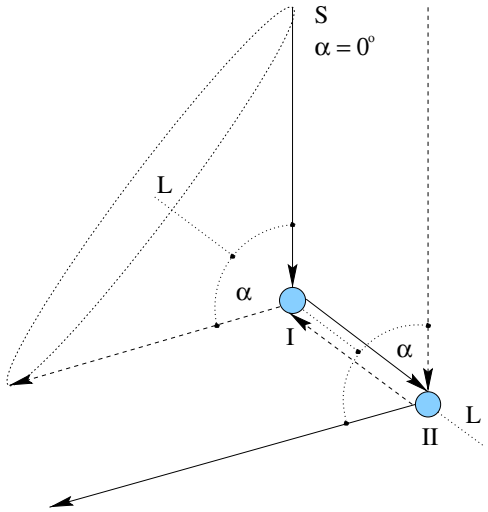

Figure 1. Coherent backscattering mechanism for the intensity surge. The wave scattered through source S → scatterer I → scatterer II → cone with axis L interferes constructively with the wave scattered through source S → scatterer II → scatterer I → cone with axis L. The backscattering direction is on the cone for arbitrary scatterers I and II, and configurational averaging results in enhanced backscattering.

direction [40]. The present technique allows the computation of full angular dependences of the backscattering peaks and polarization surges.

In section 2, the necessary multiple scattering theory and numerical techniques are described, with special emphasis on both qualitative and quantitative understanding of coherent backscattering by random media. Section 3 includes the application of the technique to plane-parallel random media of spherical scatterers within and beyond the Rayleigh regime. In section 4, the paper is closed by conclusions and remarks on future prospects.

2. Scattering theory and numerical techniques

The current study is based on approximate vector multiple scattering theory that consists of the radiative transfer (the ladder terms of the diagrammatic presentation) and coherent backscattering parts (the maximally crossed terms). We refer the reader to literature for the details of the theory (e.g., [41–47]). In the numerical technique at hand, the computation of coherent backscattering by absorbing and scattering media is carried out besides an MC radiative transfer solution for the Stokes parameters of scattered intensity [12, 48].

2.1. Coherent backscattering mechanism

The explanation of the negative polarization surge observed for many planetary-system objects based on the coherent backscattering mechanism [2, 6] is not widely known. Yet, the spatial anisotropy of the coherent backscattering cone can be interpreted analogously, providing an explanation differing from that in [22]. Curiously, the recent explanation put forward by Iwai for the spatial anisotropy [36] resembles the explanation reviewed below.

The coherent backscattering mechanism for the opposition effect is described in figure 1 for second-order scattering, readily applicable to any order of multiple scattering.

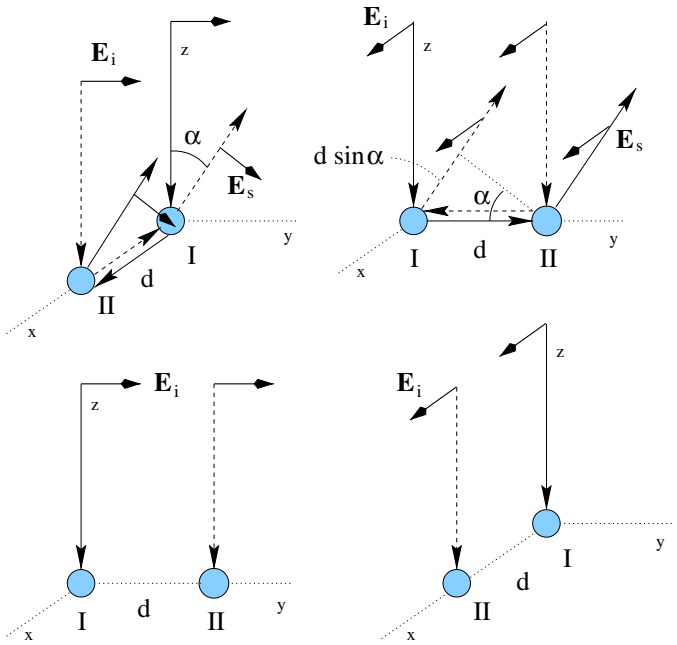

Figure 2. Coherent backscattering mechanism for the polarization surge. The four geometries represent a simplified picture of orientational averaging for unpolarized incident light. For positively polarizing single scattering, e.g., Rayleigh scattering only the two topmost geometries contribute to the coherent backscattering signal in the yz-plane at phase angle α, with differing interference characteristics. Configurational averaging favours the negatively polarizing geometry (no phase shift; top left) over the positively polarizing geometry (phase shift $kd\sin\alpha$ for wave number k and scatterer distance d; top right).

An electromagnetic plane wave is incident from the top and is represented by the solid and dashed lines. The wave interacts with two scatterers I and II, which are of the order of the wavelength λ to hundreds of wavelengths (or more) apart before travelling to the observer to the left. The two scattered wave components deriving from the two opposite propagation directions between the scatterers interfere constructively in the conical directions defined by a rotation of the light source direction S about the axis L joining the two end scatterers. Figure 1 illustrates a scattering direction on the cone precisely on the other side of the light source direction. Consequently, the backward direction (phase angle $\alpha = 0^\circ$) is on the constructive-interference cone for arbitrary locations of the two scatterers. In other directions, interference varies from constructive to destructive. Three-dimensional averaging over scatterer locations results in an opposition effect. The angular width of the effect decreases for increasing orders of interactions, because of the increasing average distance between the end scatterers.

The coherent backscattering mechanism for the negative degree of linear polarization is illustrated for second-order scattering in figure 2 using a simplified geometrical configuration of the scatterers. The incident radiation is unpolarized (e.g., the Sun), requiring the derivation and proper averaging of the Stokes parameters of the scattered electromagnetic fields ($\boldsymbol{E}_\mathrm{s}$) for two mutually perpendicular polarization states of the incident plane wave ($\boldsymbol{E}_\mathrm{i}$). In figure 2, incident linear polarizations parallel and perpendicular to the scattering plane (here yz-plane) are treated in the two leftmost and two rightmost geometries, respectively.

Thus, in figure 2, the incident plane wave interacts with two scatterers I and II at a distance d from one another aligned either on the x-axis or on the y-axis, while the observer is in the yz-plane. For the present geometries, the constructive interference cones of figure 1 reduce to the yz and xz-planes, depending on the alignment of the scatterers. Since first-order Rayleigh scattering as well as Fresnel reflection is positively polarized, the scatterers sufficiently far away from each other ($kd = 2\pi d/\lambda \gg 1$, where k and λ are the wave number and wavelength) interact predominantly with the electric field vector perpendicular to the plane defined by the source and the scatterers (two upper geometries), while interaction with the electric field vector parallel to that plane is suppressed (two lower geometries). The observer in the yz-plane will measure negative polarization from the upper left geometry in figure 2, and positive polarization from the upper right geometry. However, the positive polarization suffers from the phase difference $kd \sin\alpha$, whereas the phase difference for the negative polarization is zero for all phase angles. Averaging over the simple configurations of figure 2 or, rigorously, three-dimensional averaging over scatterer locations will result in negative polarization near the backward direction. Scattering orders higher than the second experience similar preferential interaction geometries, and contribute to negative polarization. As above for the opposition effect, the contributions from increasing orders of scattering manifest themselves at decreasing phase angles.

The present explanation of the negative polarization surge for positively polarizing single scattering constitutes, after evident modifications, an explanation of the positive polarization surge for negatively polarizing single scattering. As pointed out theoretically in [49] for second-order scattering, positive polarization surges follow for random media of spherical particles with certain optical properties. The positive polarization surges have yet to be detected in laboratory experiments.

2.2. Phases and amplitudes of coherently backscattering waves

For the computation of coherent backscattering, we sum up the electromagnetic fields that are directly and reversely scattered along the same path between the two end scatterers. The reciprocity relation ties together the phases of the two waves in the backscattering direction, allowing for the correct mutual phasing of the waves incident on the end scatterers in the direct and reverse directions. Utilization of the Jones amplitude scattering matrices for the final scattering processes guarantees that the two waves are correctly phased in all scattering directions. The amplitudes and phase differences of the direct waves follow from the radiative transfer computation. The relative amplitudes and phase differences of the reverse waves follow from a radiative-transfer-like computation along the reverse paths. The precise amplitudes of the reverse waves, and the phase difference between the direct and reverse waves, follow from the reciprocity relation in the backscattering direction.

Denote the directly scattered transverse field by $a_\perp$, $a_\parallel$, δ, $\delta_\perp$, and $\delta_\parallel$ ($a_\perp$, $a_\parallel \geqslant 0$) and the reversely scattered transverse field by $b_\perp$, $b_\parallel$, γ, $\gamma_\perp$, and $\gamma_\parallel$ ($b_\perp$, $b_\parallel \geqslant 0$) in a certain reference coordinate system $\boldsymbol{e}_\perp$, $\boldsymbol{e}_\parallel$,

$$\begin{aligned} \boldsymbol{E}_\mathrm{a} &= a_\perp \exp(\mathrm{i}\delta + \mathrm{i}\delta_\perp)\boldsymbol{e}_\perp + a_\parallel \exp(\mathrm{i}\delta + \mathrm{i}\delta_\parallel)\boldsymbol{e}_\parallel, \\ \boldsymbol{E}_\mathrm{b} &= b_\perp \exp(\mathrm{i}\gamma + \mathrm{i}\gamma_\perp)\boldsymbol{e}_\perp + b_\parallel \exp(\mathrm{i}\gamma + \mathrm{i}\gamma_\parallel)\boldsymbol{e}_\parallel. \end{aligned} \tag{1}$$

For convenience, we have introduced the phases δ and γ due to the propagation paths of the fields $\boldsymbol{E}_\mathrm{a}$ and $\boldsymbol{E}_\mathrm{b}$, respectively. The phase differences between the intrinsic field components are $\Delta\delta = \delta_\parallel - \delta_\perp$ and $\Delta\gamma = \gamma_\parallel - \gamma_\perp$.

The Stokes parameters of the $\boldsymbol{E}_{\rm a}$ field (analogously for the $\boldsymbol{E}_{\rm b}$ field) are defined by

$$\boldsymbol{I} = \begin{pmatrix} I \\ Q \\ U \\ V \end{pmatrix} = \begin{pmatrix} a_\parallel^2 + a_\perp^2 \\ a_\parallel^2 - a_\perp^2 \\ 2a_\parallel a_\perp \cos\Delta\delta \\ -2a_\parallel a_\perp \sin\Delta\delta \end{pmatrix}. \tag{2}$$

The inverse relation is unambiguous except for the absolute phase of the electromagnetic wave. For $|Q| \neq I$, that is, when $a_\parallel \neq 0$ and $a_\perp \neq 0$,

$$a_\perp = \sqrt{\frac{I+Q}{2}}, \qquad \cos\Delta\delta = \frac{U}{\sqrt{I^2-Q^2}}, \qquad a_\parallel = \sqrt{\frac{I-Q}{2}}, \qquad \sin\Delta\delta = \frac{-V}{\sqrt{I^2-Q^2}}. \tag{3}$$

For $|Q| = I$, that is, when either $a_\parallel = 0$ or $a_\perp = 0$, we set $\Delta\delta = 0$.

The Stokes parameters of the total field $\boldsymbol{E} = \boldsymbol{E}_{\rm a} + \boldsymbol{E}_{\rm b}$ are

$$\boldsymbol{I} = \boldsymbol{I}^{\rm RT} + \boldsymbol{I}^{\rm C}, \tag{4}$$

where the radiative transfer (superscript 'RT') and coherent backscattering ('C') parts are

$$\begin{aligned} \boldsymbol{I}^{\rm RT} &= \begin{pmatrix} \frac{1}{2}\left(a_\parallel^2 + a_\perp^2 + b_\parallel^2 + b_\perp^2\right) \\ \frac{1}{2}\left(a_\parallel^2 - a_\perp^2 + b_\parallel^2 - b_\perp^2\right) \\ a_\parallel a_\perp \cos\Delta\delta + b_\parallel b_\perp \cos\Delta\gamma \\ -a_\parallel a_\perp \sin\Delta\delta - b_\parallel b_\perp \sin\Delta\gamma \end{pmatrix}, \\ \boldsymbol{I}^{\rm C} &= \begin{pmatrix} a_\perp b_\perp \cos(\Delta\epsilon + \delta_\perp - \gamma_\perp) + a_\parallel b_\parallel \cos(\Delta\epsilon + \Delta\delta - \Delta\gamma + \delta_\perp - \gamma_\perp) \\ -a_\perp b_\perp \cos(\Delta\epsilon + \delta_\perp - \gamma_\perp) + a_\parallel b_\parallel \cos(\Delta\epsilon + \Delta\delta - \Delta\gamma + \delta_\perp - \gamma_\perp) \\ a_\perp b_\parallel \cos(\Delta\epsilon - \Delta\gamma + \delta_\perp - \gamma_\perp) + a_\parallel b_\perp \cos(\Delta\epsilon + \Delta\delta + \delta_\perp - \gamma_\perp) \\ a_\perp b_\parallel \sin(\Delta\epsilon - \Delta\gamma + \delta_\perp - \gamma_\perp) - a_\parallel b_\perp \sin(\Delta\epsilon + \Delta\delta + \delta_\perp - \gamma_\perp) \end{pmatrix}. \end{aligned} \tag{5}$$

Here $\Delta\epsilon$ is the phase difference due to the differing propagation paths,

$$\Delta\epsilon = \delta - \gamma = k(\boldsymbol{e}_{\rm i} + \boldsymbol{e}_{\rm s}) \cdot (\boldsymbol{r}_{\rm s} - \boldsymbol{r}_{\rm i}), \tag{6}$$

where $\boldsymbol{e}_{\rm i}$ and $\boldsymbol{e}_{\rm s}$ are the propagation directions of the incident and scattered waves and $\boldsymbol{r}_{\rm i}$ and $\boldsymbol{r}_{\rm s}$ are the locations of the end scatterers.

The coherent backscattering part in equation (5) is expressed using the known phase differences $\Delta\delta$, $\Delta\gamma$, and $\Delta\epsilon$ and the phase difference $\delta_\perp - \gamma_\perp$ that is unknown. If $\delta_\perp(0)$ and $\gamma_\perp(0)$ are the phases in the backscattering direction and $\eta = \gamma_\perp(0) - \delta_\perp(0)$,

$$\delta_\perp - \gamma_\perp = [\delta_\perp - \delta_\perp(0)] - [\gamma_\perp - \gamma_\perp(0)] - \eta. \tag{7}$$

As the phases $\delta_\perp - \delta_\perp(0)$ and $\gamma_\perp - \gamma_\perp(0)$ are relative and available from the amplitude scattering matrix algebras for the fields $\boldsymbol{E}_{\rm a}$ and $\boldsymbol{E}_{\rm b}$, the phase η emerges as being the one and only unknown phase in the computation.

In what follows, the phase η is determined using the reciprocity principle. In the backscattering direction, because of the coinciding propagation paths, $\Delta\epsilon = 0$ in equation (5). According to the reciprocity principle in general, the amplitude scattering matrices of arbitrary reciprocally propagating waves are interrelated by [38–40]

$$\boldsymbol{S}(-\boldsymbol{e}_{\rm i}, -\boldsymbol{e}_{\rm s}) = \boldsymbol{Q}\boldsymbol{S}^T(\boldsymbol{e}_{\rm s}, \boldsymbol{e}_{\rm i})\boldsymbol{Q}, \tag{8}$$

where

$$\boldsymbol{S} = \begin{pmatrix} S_{\perp\perp} & S_{\perp\parallel} \\ S_{\parallel\perp} & S_{\parallel\parallel} \end{pmatrix}, \qquad \boldsymbol{Q} = \begin{pmatrix} 1 & 0 \\ 0 & -1 \end{pmatrix}. \tag{9}$$

Combined Mueller and Jones matrix algebra in the reverse propagation direction allows the computation of an unnormalized field $\tilde{b}_\perp$, $\tilde{b}_\parallel$, $\tilde{\gamma}$, $\tilde{\gamma}_\perp$, and $\tilde{\gamma}_\parallel$ so that the phase differences $\Delta\tilde{\gamma} = \tilde{\gamma}_\parallel - \tilde{\gamma}_\perp = \Delta\gamma$, that is, the polarization properties of the reverse wave are available. What is left is the scaling of the amplitudes $\tilde{b}_\perp$ and $\tilde{b}_\parallel$ and the shifting of the phases $\tilde{\gamma}_\perp$ and $\tilde{\gamma}_\parallel$ so that the reciprocity relation is fulfilled. Now the reciprocity relation in equation (8) gives a complex-valued renormalization coefficient to be applied to the $\tilde{b}$-field. After writing the directly and reversely backscattered waves using the amplitude scattering matrix formalism and subtracting the expressions from one another, the renormalization coefficient C emerges as the ratio (the subscript 'i' refers to the original field incident on the medium)

$$\begin{aligned} C &= \frac{a_\perp(0)a_{i,\perp}\exp(\mathrm{i}\delta_\perp(0)+\mathrm{i}\delta_{i,\perp}) - a_\parallel(0)a_{i,\parallel}\exp(\mathrm{i}\delta_\parallel(0)+\mathrm{i}\delta_{i,\parallel})}{\tilde{b}_\perp(0)a_{i,\perp}\exp(\mathrm{i}\tilde{\gamma}_\perp(0)+\mathrm{i}\delta_{i,\perp}) - \tilde{b}_\parallel(0)a_{i,\parallel}\exp(\mathrm{i}\tilde{\gamma}_\parallel(0)+\mathrm{i}\delta_{i,\parallel})} \\ &= |C|\exp(\mathrm{i}\eta), \end{aligned} \tag{10}$$

giving $|C|$ and η as a function of known phases and amplitudes. It then follows that the wave incident on the final scatterer in the reverse direction can be re-amplified by $|C|$ and phase-shifted by η in order to fulfil the reciprocity relation after the scattering process in the backscattering direction. In the renormalization, the optical depths of the direct and reverse waves have to be carefully accounted for.

Consequently, the properly renormalized reverse wave component and the direct wave component can be used in the computation of the angular profiles in both intensity and polarization close to the backscattering direction. The absolute electromagnetic phase is computed for neither directly nor reversely propagating components; instead, the phase difference between their phase differences is properly reset in the backscattering direction, leaving the absolute phase as an arbitrary number having no influence on the results.

In principle, there are geometrical configurations of the incident and scattered fields that, strictly, cannot be treated using the reciprocity relation. One advantage of the MC technique is the fact that, in practice, these singular geometries have a vanishing probability of occurrence in the computation.

Note that ensemble-averaged scattering matrices cannot be utilized in the coherent backscattering computations, because such matrices are typically unpolarizing: at each scattering event, the Stokes parameters of scattered light have to correspond to electromagnetic field components with a well-defined phase difference. Indeed, it is possible to replace the 4×4 Mueller-matrix algebra unambiguously by a 2×2 Jones-matrix algebra.

2.3. Scattering theory

For spherical scatterers, the extinction, scattering, and absorption efficiencies and the single-scattering albedo are [39]

$$\begin{aligned} q_\mathrm{s} &= \frac{2}{x^2}\sum_{l=1}^{\infty}(2l+1)(|a_l|^2+|b_l|^2), & q_\mathrm{e} &= \frac{2}{x^2}\sum_{l=1}^{\infty}(2l+1)\mathrm{Re}(a_l+b_l), \\ q_\mathrm{a} &= q_\mathrm{e} - q_\mathrm{s}, & \tilde{\omega} &= \frac{q_\mathrm{s}}{q_\mathrm{e}}, \end{aligned} \tag{11}$$

where a_l and b_l are the vector spherical harmonics coefficients of the scattered electromagnetic field, depending on the size parameter $x = ka$ (a is radius) and the complex refractive index m of the spherical scatterers:

$$a_l = \frac{m\psi_l(mx)\psi_l'(x) - \psi_l(x)\psi_l'(mx)}{m\psi_l(mx)\xi_l'(x) - \xi_l(x)\psi_l'(mx)}, \qquad b_l = \frac{\psi_l(mx)\psi_l'(x) - m\psi_l(x)\psi_l'(mx)}{\psi_l(mx)\xi_l'(x) - m\xi_l(x)\psi_l'(mx)}. \tag{12}$$

Here ψ_l and ξ_l are Riccati–Bessel functions and strictly related to the spherical Bessel and Hankel functions j_l and $h_l^{(1)}$,

$$\psi_l(x) = x j_l(x), \qquad \xi_l(x) = x h_l^{(1)}(x). \tag{13}$$

The normalized scattering phase matrix, below briefly scattering matrix, is

$$\begin{aligned} \boldsymbol{P} &= \frac{2}{x^2 q_\mathrm{s}} \begin{pmatrix} |S_{\parallel\parallel}|^2 + |S_{\perp\perp}|^2 & |S_{\parallel\parallel}|^2 - |S_{\perp\perp}|^2 & 0 & 0 \\ |S_{\parallel\parallel}|^2 - |S_{\perp\perp}|^2 & |S_{\parallel\parallel}|^2 + |S_{\perp\perp}|^2 & 0 & 0 \\ 0 & 0 & \mathrm{Re}(S_{\perp\perp}^* S_{\parallel\parallel}) & \mathrm{Im}(S_{\perp\perp}^* S_{\parallel\parallel}) \\ 0 & 0 & -\mathrm{Im}(S_{\perp\perp}^* S_{\parallel\parallel}) & \mathrm{Re}(S_{\perp\perp}^* S_{\parallel\parallel}) \end{pmatrix}, \\ N_{11} &= \int_{4\pi} \frac{\mathrm{d}\Omega}{4\pi} P_{11}(\Omega) = 1, \qquad g_{11} = \int_{4\pi} \frac{\mathrm{d}\Omega}{4\pi} \cos\theta P_{11}(\Omega), \end{aligned} \tag{14}$$

where the amplitude scattering matrix elements $S_{\perp\perp}$ and $S_{\parallel\parallel}$ are

$$\begin{aligned} S_{\perp\perp} &= \sum_{l=1}^{\infty} \frac{2l+1}{l(l+1)} \left[a_l \frac{\mathrm{d}P_l^1(\cos\theta)}{\mathrm{d}\theta} + b_l \frac{1}{\sin\theta} P_l^1(\cos\theta) \right], \\ S_{\parallel\parallel} &= \sum_{l=1}^{\infty} \frac{2l+1}{l(l+1)} \left[a_l \frac{1}{\sin\theta} P_l^1(\cos\theta) + b_l \frac{\mathrm{d}P_l^1(\cos\theta)}{\mathrm{d}\theta} \right], \end{aligned} \tag{15}$$

and P_l^1 are associated Legendre functions. The norm of the phase function is $N_{11} = 1$, and g_{11} is its asymmetry parameter (see also equations (30) and (31)).

In the Rayleigh limit of light scattering by spherical particles, the scattering and absorption efficiencies are reduced to [39]

$$q_\mathrm{s} = \frac{8}{3} x^4 \left| \frac{m^2 - 1}{m^2 + 2} \right|^2, \qquad q_\mathrm{a} = 4x \,\mathrm{Im}\left(\frac{m^2 - 1}{m^2 + 2} \right), \tag{16}$$

and the scattering matrix is

$$\boldsymbol{P} = \frac{3}{2} \begin{pmatrix} \frac{1}{2}(1 + \cos^2\theta) & -\frac{1}{2}\sin^2\theta & 0 & 0 \\ -\frac{1}{2}\sin^2\theta & \frac{1}{2}(1 + \cos^2\theta) & 0 & 0 \\ 0 & 0 & \cos\theta & 0 \\ 0 & 0 & 0 & \cos\theta \end{pmatrix}. \tag{17}$$

For the physical quantities in multiple scattering, definitions in [50] are followed. The specific intensity of the incident radiation (in units of J m^{-2} s^{-1} sr^{-1}) is

$$\boldsymbol{I}_0(\mu, \phi) = \pi \boldsymbol{F}_0 \delta(\mu - \mu_0) \delta(\phi - \phi_0), \tag{18}$$

where $\pi \boldsymbol{F}_0$ is the incident flux density (in units of J m^{-2} s^{-1}) and $\mu_0 = \cos\iota$. ι and ϕ_0 are the angle of incidence (measured from the outward normal of the plane-parallel medium) and the azimuthal angle, respectively.

The 4×4 reflection coefficient matrix $\boldsymbol{R}$, below briefly reflection matrix, relates the incident flux density and the specific intensity of reflected radiation as

$$\begin{aligned} &\boldsymbol{I}_\mathrm{r}(\mu, \phi) = \mu_0 \boldsymbol{R}(\mu, \mu_0, \phi - \phi_0) \boldsymbol{F}_0, \\ &\boldsymbol{R}(\mu, \mu_0, \phi - \phi_0) = \boldsymbol{R}^\mathrm{RT}(\mu, \mu_0, \phi - \phi_0) + \boldsymbol{R}^C(\mu, \mu_0, \phi - \phi_0), \end{aligned} \tag{19}$$

where $\mu = \cos\epsilon$. ϵ and ϕ are the angle of emergence (measured from the outward normal of the plane-parallel medium) and the azimuthal angle, respectively. The matrix element R_{11} corresponds to the so-called reflection coefficient in scalar radiative transfer. The enhancement factor is

$$\zeta(\mu, \mu_0, \phi - \phi_0) = \frac{R_{11}(\mu, \mu_0, \phi - \phi_0)}{R_{11}^\mathrm{RT}(\mu_0, \mu_0, 0)}. \tag{20}$$

The degree of linear polarization is $P = -\tilde{R}_{21}/\tilde{R}_{11}$, where $\tilde{\boldsymbol{R}}$ is the reflection matrix expressed in the scattering plane defined by the source, object and the observer.

The plane albedo $A_{\rm p}(\mu_0)$ is the fraction of the incident flux which is reflected by the plane-parallel medium in the case of incident unpolarized radiation,

$$A_{\rm p}(\mu_0) = \frac{1}{\pi}\int_0^1\int_0^{2\pi} {\rm d}\mu\,{\rm d}\phi\,\mu R_{11}^{\rm RT}(\mu,\mu_0,\phi-\phi_0). \tag{21}$$

Note that the plane albedo here refers to the radiative transfer part only. The current treatment of energy conservation is sufficient for narrow coherent backscattering peaks.

Extinction is assumed to be exponential within the random medium. The optical depth τ_s between two locations a distance s apart is computed using the scalar extinction coefficient $k_{\rm e}$,

$$\tau_s = \int_0^s {\rm d}s\,k_{\rm e} = k_{\rm e}s = \frac{s}{\ell}, \qquad \ell = \frac{1}{k_{\rm e}}, \tag{22}$$

where ℓ is the extinction mean free path. If n and v are the number and volume densities of scatterers with radii a in a discrete random medium, we obtain

$$k_{\rm e} = nq_{\rm e}\pi a^2 = \frac{3vq_{\rm e}}{4a}, \qquad n = \frac{3v}{4\pi a^3}. \tag{23}$$

2.4. Randomizing scattering angles

Of interest in MC multiple scattering computations is the generation of scattering angles in each scattering process. Here we outline an efficient technique for block-diagonal scattering matrices enabled by the Stokes parameter formulation, with prospects for generalization to more complicated matrices. For example, as it stands below, the technique is already applicable to radiative transfer computations utilizing the block-diagonal ensemble-averaged scattering matrices such as those of Gaussian particles [51].

We denote the Stokes parameters of the incoming and outgoing rays by $\boldsymbol{I}_1 = (I_1, Q_1, U_1, V_1)^T$ and $\boldsymbol{I}_2 = (I_2, Q_2, U_2, V_2)^T$, respectively, and assume that the reference system of the incoming ray is arbitrary. The outgoing ray in the reference system of the local scattering plane is given by

$$\boldsymbol{I}_2 \propto \boldsymbol{P}(\theta,\phi)\cdot\boldsymbol{K}(\phi)\cdot\boldsymbol{I}_1, \tag{24}$$

where $\boldsymbol{K}$ is a 4×4 Mueller matrix for the rotation to the scattering plane, $\boldsymbol{P}$ is the 4×4 Mueller matrix for scattering (scattering matrix), and θ and ϕ are the temporary scattering angles in the reference system of $\boldsymbol{I}_1$.

The Monte Carlo generation of the scattering angles is based on the angular intensity distribution $I_2(\theta,\phi)$; i.e.,

$$\begin{aligned} I_2(\theta,\phi) \propto{}& I_1P_{11}(\theta,\phi) + Q_1[P_{12}(\theta,\phi)\cos2\phi + P_{13}(\theta,\phi)\sin2\phi] \\ &+ U_1[-P_{12}(\theta,\phi)\sin2\phi + P_{13}(\theta,\phi)\cos2\phi] + V_1P_{14}(\theta,\phi). \end{aligned} \tag{25}$$

For scattering by spherical particles, the scattering matrix is independent of the azimuthal scattering angle ϕ and $P_{13} = P_{14} = 0$, so we obtain

$$I_2(\theta,\phi) \propto I_1P_{11}(\theta) + Q_1P_{12}(\theta)\cos2\phi - U_1P_{12}(\theta)\sin2\phi. \tag{26}$$

The azimuthal angle ϕ shows up only in the rotation, and $I_2(\theta,\phi)$ is independent of the Stokes parameter V_1.

In order to obtain the probability density function $p(\theta,\phi)$, we normalize $I_2(\theta,\phi)$ and obtain

$$p(\theta,\phi) = \frac{1}{4\pi}P_{11}(\theta) + \frac{1}{4\pi}P_{12}(\theta)\left(\frac{Q_1}{I_1}\cos2\phi - \frac{U_1}{I_1}\sin2\phi\right). \tag{27}$$

The marginal probability density for θ is

$$p(\theta) = \frac{1}{2} P_{11}(\theta) \tag{28}$$

and thus independent of $\boldsymbol{I}_1$. For ϕ, it is more complicated and depends on $\boldsymbol{I}_1$:

$$p(\phi) = \frac{1}{2\pi} + \left(\frac{Q_1}{I_1} \cos 2\phi - \frac{U_1}{I_1} \sin 2\phi \right) \frac{1}{4\pi} \int_0^\pi \mathrm{d}\theta \sin\theta P_{12}(\theta). \tag{29}$$

Curiously, the integral on the right gives rise for a polarization norm,

$$N_{12} = -\frac{1}{2} \int_0^\pi \mathrm{d}\theta \sin\theta P_{12}(\theta), \tag{30}$$

which can be used to measure, first, whether the scatterers are net positively or negatively polarizing and, second, how efficiently they can polarize incident unpolarized light. For Rayleigh scatterers, $N_{12} = \frac{1}{2}$ (cf the phase function norm $N_{11} = 1$ in equation (14)). Note that the polarization asymmetry parameter can be defined as

$$g_{12} = -\frac{1}{2} \int_0^\pi \mathrm{d}\theta \sin\theta \cos\theta P_{12}(\theta). \tag{31}$$

For Rayleigh scatterers, $g_{12} = 0$.

The practical generation of θ and ϕ can be carried out using, first, $p(\theta)$ to obtain the sample polar scattering angle $\tilde{\theta}$ and, second, the conditional probability

$$p(\phi \mid \tilde{\theta}) = \frac{p(\tilde{\theta}, \phi)}{p(\tilde{\theta})} = \frac{1}{2\pi} \left[1 + \frac{P_{12}(\tilde{\theta})}{P_{11}(\tilde{\theta})} \left(\frac{Q_1}{I_1} \cos 2\phi - \frac{U_1}{I_1} \sin 2\phi \right) \right] \tag{32}$$

to obtain the sample azimuthal scattering angle $\tilde{\phi}$.

For the Rayleigh scattering matrix in equation (17), we obtain $\tilde{\theta}$-values analytically from

$$\cos\tilde{\theta} = \sqrt[3]{\sqrt{1+y^2} + y} - \sqrt[3]{\sqrt{1+y^2} - y}, \tag{33}$$

where y is a uniform random deviate $y \in]-2, 2[$. For spherical scatterers beyond the Rayleigh regime, the generation of $\tilde{\theta}$ can best be carried out via interpolation in a precomputed table of $\cos\tilde{\theta}$-values as a function of $y \in]0, 1[$.

For the subsequent generation of $\tilde{\phi}$, denote

$$e\cos\gamma = -\frac{P_{12}(\tilde{\theta})}{P_{11}(\tilde{\theta})} \frac{Q_1}{I_1}, \qquad e\sin\gamma = -\frac{P_{12}(\tilde{\theta})}{P_{11}(\tilde{\theta})} \frac{U_1}{I_1}, \tag{34}$$

where

$$e = \sqrt{\frac{P_{12}^2(\tilde{\theta})}{P_{11}^2(\tilde{\theta})} \frac{Q_1^2 + U_1^2}{I_1^2}} \tag{35}$$

and the angle γ is unambiguously determined by equation (34). Then, the probability density function is

$$p(\phi|\tilde{\theta}) = \frac{1}{2\pi} \left[1 - e\cos(2\phi + \gamma) \right], \tag{36}$$

and the cumulative distribution function is

$$P(\phi \mid \tilde{\theta}) = \frac{1}{2\pi} \left[\phi - \frac{1}{2} e \sin(2\phi + \gamma) + \frac{1}{2} e \sin\gamma \right]. \tag{37}$$

For generating $\tilde{\phi}$, we thus obtain (with $y \in]0, 1[$ a uniform random deviate)

$$(2\tilde{\phi} + \gamma) - e\sin(2\tilde{\phi} + \gamma) = 4\pi y + \gamma - e\sin\gamma, \tag{38}$$

that is, Kepler's equation $E - e\sin E = M$ with 'eccentric anomaly' $E = 2\tilde{\phi} + \gamma$, 'eccentricity' e, and 'mean anomaly' $M = 4\pi y + \gamma - e\sin\gamma$. Kepler's equation can be solved for $\tilde{\phi}$ efficiently using Newton's technique [52]: typically, only a few iterations are necessary to obtain $\tilde{\phi}$ with sufficient accuracy and the generation is next-to analytical.

2.5. Summary of numerical technique

The vector radiative transfer part of the numerical MC technique has been carefully verified using reference results for a Rayleigh-scattering planetary atmosphere [53]. Entire reflection matrices are computed by repeating the analysis for varying Stokes parameters of incident light. Whereas close-packing effects can be approximately accounted for by, e.g., the structure factor formalism, we constrain our computations to volume densities less than 10% to avoid such corrections.

The reversely propagating waves exhibit peculiar polarization characteristics as a function of the scattering order. The polarization state of the directly propagating wave changes at each additional scattering process, but the state of the reversely propagating wave converges after a number of scatterings. In other words, the scattering processes at the end of the reverse path tend to control the overall polarization properties of the reverse wave, and the scatterers constitute an efficient reverse polarizer. The convergence of the polarization state is here utilized to speed up the computations of the coherent backscattering contribution.

An essential feature of the numerical technique is the *a priori* selection of reflection/transmission directions for updating Stokes parameters during the MC radiative transfer computation, thus avoiding collection of rays into finite bins. Fixed angles allow for the computation of electromagnetic phase differences and thus the coherent backscattering effect. In the technique, there are two sets of fixed angles. First, the radiative transfer set utilizes Gauss–Legendre abscissae and weights for the polar angle and uniform spacing for the azimuthal angle [54]. Second, the coherent backscattering set can be chosen to cover any angular domain necessary.

In the backscattering reference frame, where the z-axis points in the direction of the source, two angular schemes A-I and A-II are incorporated for the coherent backscattering computations. In both schemes, the azimuthal angle is uniformly spaced with maximum four angles. In A-I, the backscattering angle takes the 23 values of $\alpha = 0.0^\circ, 0.05^\circ, 0.1^\circ, 0.15^\circ, 0.2^\circ, 0.25^\circ, 0.5^\circ, 1.0^\circ, 1.5^\circ, 2.0^\circ, 2.5^\circ, 3.0^\circ, 4.5^\circ, 6.0^\circ, 7.5^\circ, 9.0^\circ, 12.0^\circ, 15.0^\circ, 18.0^\circ, 21.0^\circ, 24.0^\circ, 27.0^\circ$, and 30.0°. The A-II scheme has a finer angular resolution and takes the 26 values of $\alpha = 0.0^\circ, 0.005^\circ, 0.01^\circ, 0.015^\circ, 0.02^\circ, 0.025^\circ, 0.05^\circ, 0.1^\circ, 0.15^\circ, 0.2^\circ, 0.25^\circ, 0.3^\circ, 0.45^\circ, 0.6^\circ, 0.75^\circ, 0.9^\circ, 1.2^\circ, 1.5^\circ, 1.8^\circ, 2.1^\circ, 2.4^\circ, 2.7^\circ, 3.0^\circ, 4.0^\circ, 5.0^\circ$, and 6.0°.

In the generation of new propagation directions, Kepler's equation is efficiently solved using Newton's method. Within the media, due to constant updating of the Stokes parameters of reflected light, the generation of propagation directions is coupled with the generation of the propagation path lengths, confining the subsequent scattering processes into the scattering medium.

3. Results and discussion

In order to evaluate the number of rays needed for acceptable numerical accuracy, computations were carried out for plane-parallel media of Rayleigh scatterers with $\tilde{\omega} = 0.9$ and $k\ell = 300$ (figure 3, angular scheme A-I) using 10, 10^2, 10^3, 10^4, 10^5 and 10^6 rays. Whereas 10^2 rays can already give a rough idea of the main features, of the order of 10^5 rays are required to reach acceptable convergence. A small offset of R_{12} from zero is typically found in the backscattering direction for normal incidence. The offset vanishes with increasing number of rays, and is here subtracted from the polarization curves across the angular regime close to backscattering—the legitimacy of the subtraction is supported by the coinciding polarization surges in figure 3 for

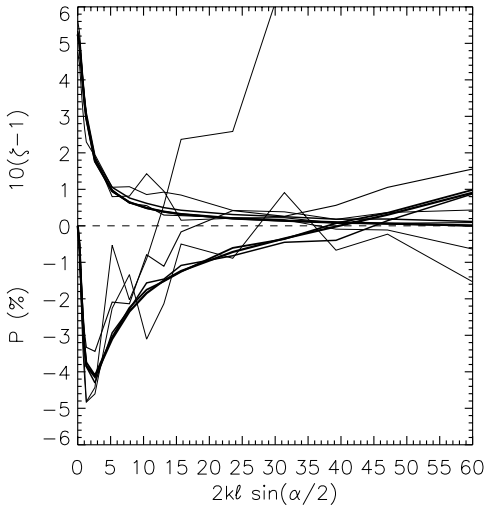

Figure 3. Numerical accuracy of the enhancement factors and polarization surges for plane-parallel media of Rayleigh scatterers with single-scattering albedo $\tilde{\omega} = 0.9$ and extinction mean free path $k\ell = 300$. With increasing line thickness, 10, 10^2, 10^3, 10^4, 10^5 and 10^6 rays were utilized in the computation.

large numbers of rays. Note that the characteristics are plotted against $2k\ell \sin\alpha/2 \approx k\ell\alpha$ (α small), a dimensionless quantity showing up in the coherent backscattering terms.

The polarization state of the reversely scattered waves was studied for semi-infinite plane-parallel media of spherical scatterers allowing for a maximum deviation of 10^{-12} for Stokes parameters scaled to a unit parameter I. For Rayleigh scatterers with $\tilde{\omega} = 0.99$, the distribution of scattering orders where convergence was reached turned out to be bell-shaped with the most probable scattering order for polarization convergence at 50 and the full distribution spanning orders 15–115. For scatterers beyond the Rayleigh regime with $x = 1.4$ and $m = 1.2 + \mathrm{i}10^{-4}$ (see table 2 and figure 9), the scattering order distribution was similar, evidently due to the Rayleigh-like polarization characteristics of the scatterers. For spherical scatterers with larger size parameters ($x \approx 10$), the scattering order distribution shifts considerably, spanning several hundred orders of scattering just below the order of 1000. The distributions are sensitive to the maximum deviation specified.

3.1. Rayleigh scattering

Within the Rayleigh regime, the scattering matrices are identical for all scatterers. The single-scattering albedos and extinction mean free paths can thus take values obtained by mixing Rayleigh scatterers with different physical characteristics without destroying the Rayleigh scattering matrix. In what follows, after a detailed feasibility study based on extensive computations for spherical scatterers using the software by Bohren and Huffman [39], we have chosen to make use of $k\ell = 100$, 300, 900 and $\tilde{\omega} = 0.05$, 0.1, 0.3, 0.5, 0.7, 0.9, 0.95, 0.99, 0.999, 0.9999, 1.0 (table 1). Unless otherwise stated, 10^5 rays have been traced for each case, and ray tracing has been terminated when the relative flux density falls below 10^{-6}.

Selected enhancement factors ζ and polarization surges $-R_{21}/R_{11}$ are shown in figure 4 for given $\tilde{\omega}$ and $k\ell$ in the case of normal incidence (A-I). In general, the intensity and polarization surges become narrower for increasing lengths of wave propagation paths, in accordance with

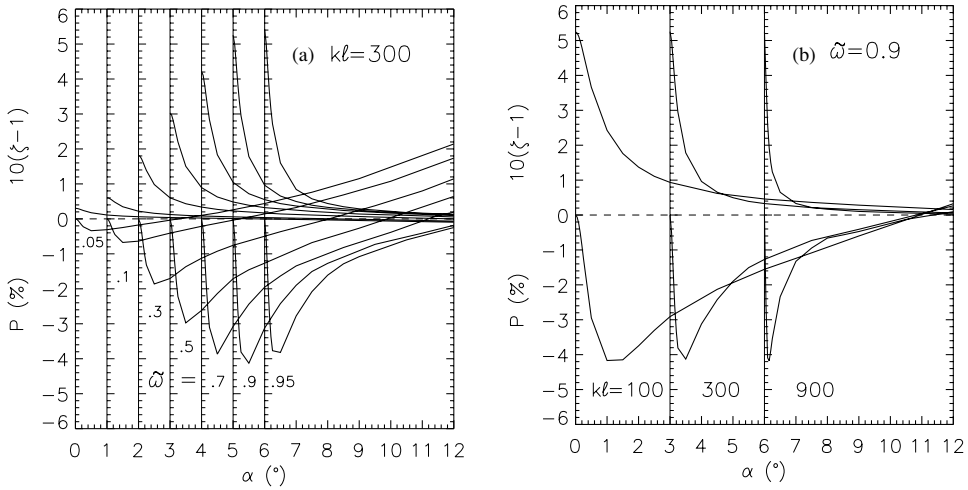

Figure 4. Enhancement factors and polarization surges for semi-infinite plane-parallel media of Rayleigh scatterers with varying single-scattering albedos $\tilde{\omega}$ and extinction mean free paths $k\ell$ (normal incidence): (a) $\tilde{\omega} = 0.05$, 0.1, 0.3, 0.5, 0.7, 0.9, 0.95 and $k\ell = 300$; (b) $\tilde{\omega} = 0.9$ and $k\ell = 100$, 300, 900. Angular scales shifted for better illustration.

Table 1. Plane albedos $A_{\rm p}$ (%), enhancement factors $\zeta(0)$ and minimum polarizations $P_{\rm min}$ (%) for plane-parallel media of given optical thickness τ_h consisting of Rayleigh scatterers with single-scattering albedo $\tilde{\omega}$ in the case of normal incidence. The extinction mean free path is $k\ell = 300$.

	$A_{\rm p}$ τ_h			$\zeta(0)$ τ_h			$P_{\rm min}$ τ_h		
$\tilde{\omega}$	2	5	∞	2	5	∞	2	5	∞
0.05	0.857	0.864	0.864	1.029	1.030	1.030	−0.32	−0.33	−0.34
0.10	1.77	1.78	1.78	1.058	1.060	1.060	−0.63	−0.68	−0.67
0.30	6.09	6.16	6.17	1.175	1.182	1.182	−1.83	−1.91	−1.86
0.50	12.0	12.3	12.3	1.290	1.303	1.303	−2.95	−3.03	−2.97
0.70	20.8	21.8	21.8	1.402	1.422	1.421	−3.91	−3.89	−3.87
0.90	36.7	42.0	42.3	1.501	1.525	1.525	−4.47	−4.12	−4.13
0.95	43.1	52.9	54.0	1.523	1.542	1.539	−4.56	−3.98	−3.94
0.99			75.3			1.552			−3.52
0.999			91.2			1.535			−3.09
0.9999			97.0			1.537			−2.83
1.0	51.5	73.6		1.543	1.553		−4.50	−3.48	

the coherent backscattering mechanism. For the darkest media with $\tilde{\omega} = 0.05$, the opposition effect is almost hidden but the negative polarization surges are clearly visible, underscoring the importance of multiple scattering even for dark samples.

Figure 5 shows both individual and cumulative contributions from different scattering orders to the entire reflection matrix for $\tilde{\omega} = 0.9$ and $k\ell = 300$ (A-I, 10^6 rays). Up to seven orders of scattering are gradually included in the computations. According to figures 5(a) and (b), the leading contribution arises from the second order, with the seventh-order contribution being roughly an order of magnitude weaker. With increasing order of scattering, the widths of the surges become narrower.

In figure 5(c), the reflection matrix element R_{22} underscores the known result that coherent backscattering tends to conserve the linear polarization state of the incident radiation. Note

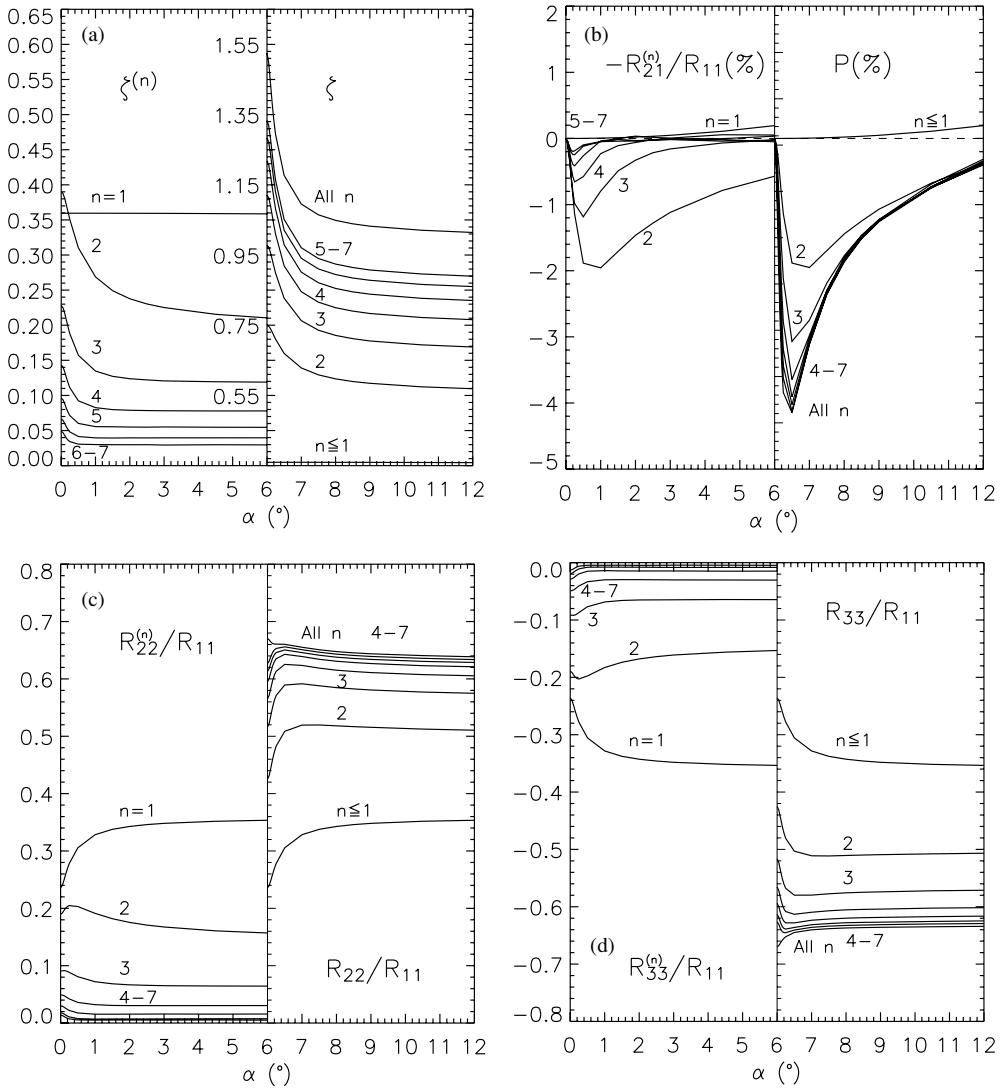

Figure 5. Individual (left) and cumulative reflection matrix elements (right) from the scattering orders $n = 1, 2, \ldots, 7$ for semi-infinite plane-parallel media of Rayleigh scatterers with $\tilde{\omega} = 0.9$ and $k\ell = 300$ (normal incidence): (a) $R_{11}^{(n)}(\alpha)/R_{11}^{\mathrm{RT}}(0)$, (b) $-R_{21}^{(n)}(\alpha)/R_{11}(\alpha)$, (c) $R_{22}^{(n)}(\alpha)/R_{11}(\alpha)$, (d) $R_{33}^{(n)}(\alpha)/R_{11}(\alpha)$, (e) $R_{44}^{(n)}(\alpha)/R_{11}(\alpha)$. Also shown are the cumulative elements from all significant orders of scattering. Note that the individual contributions have been illustrated so that they are additive.

that very high orders of scattering are needed to reverse the angular dependence close to the backscattering direction. The matrix element R_{33} (figure 5(d)) is close to a mirror image of R_{22} with respect to the zero-ordinate axis. For both R_{22} and R_{33}, the first-order contribution behaves qualitatively in a way opposite to the higher-order contributions. However, recalling that the denominator includes the abrupt coherent backscattering surge, the first-order contribution without the denominator does indeed increase towards the backscattering direction.

The reflection matrix element R_{44} (figure 5(e)) shows a mixed trend among the different orders. For the second and third orders, the contributions are negative and amplified for

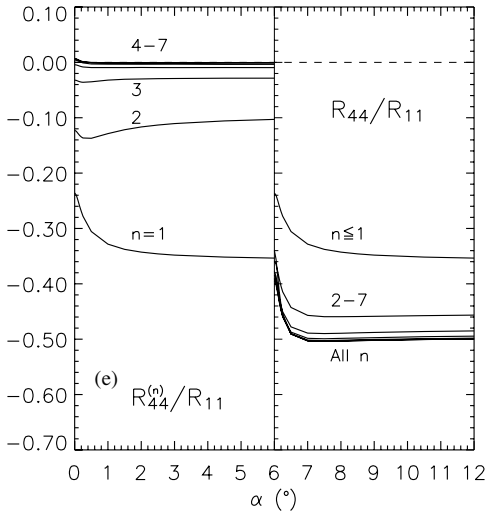

Figure 5. (Continued.)

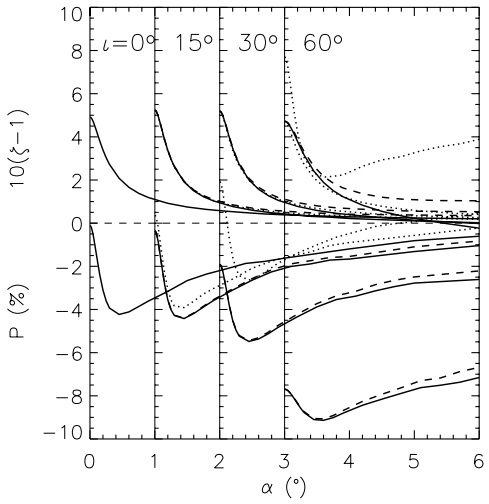

Figure 6. Enhancement factors and polarization surges for varying angles of incidence $\iota = 0°, 15°, 30°$ and $60°$ for scattering planes perpendicular (dotted line) and parallel (solid and dashed lines) to the surface normal–source direction-plane (semi-infinite media of Rayleigh scatterers with $\tilde{\omega} = 0.9$ and $k\ell = 300$). For the parallel plane, results differ in the directions towards the surface normal (dashed line) and the surface (solid line).

decreasing phase angle whereas, for the fourth order, the contribution is negative but neutralized for decreasing phase angle. For the higher orders, the contributions are positive and amplified, signalling of a weak conservation of the circular polarization state incident on the medium. The reflection matrix element R_{34} vanishes as expected for a plane-parallel medium of Rayleigh scatterers in normal incidence. To summarize, all of the backscattering characteristics in figure 5 are in agreement with the physical interpretation of the coherent backscattering mechanism reviewed in section 2.1 (figures 1 and 2).

Figure 6 shows the effects of oblique incidence angles on the backscattering surges in intensity and polarization, again for $k\ell = 300$ and $\tilde{\omega} = 0.9$ (A-II, 5×10^4 rays). The

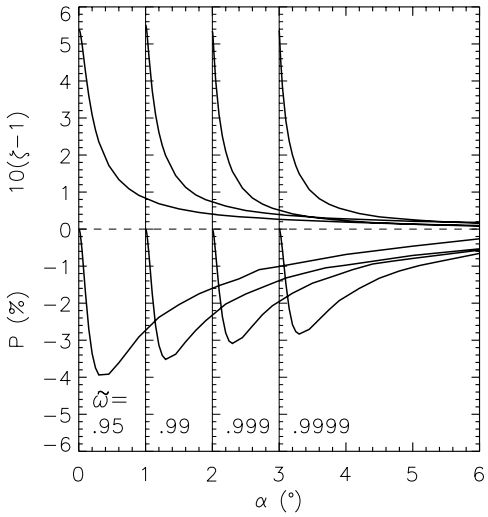

Figure 7. Enhancement factors and polarization surges for semi-infinite plane-parallel media with extinction mean free path $k\ell = 300$ composed of Rayleigh scatterers with high single-scattering albedos of $\tilde{\omega} = 0.95, 0.99, 0.999$ and 0.9999.

angle of incidence assumes four values of $\iota = 0^\circ, 15^\circ, 30^\circ$ and 60°, and backscattering characteristics are plotted in two scattering planes perpendicular to one another, crossing in the backscattering direction. For the scattering plane perpendicular to the plane defined by the directions of incidence and the outward normal vector of the medium, the results coincide on the two azimuthal angles differing 180° (in the backscattering frame). For the scattering plane coinciding with the plane defined by the normal vector and direction of incidence, the results are different for scattering directions between the backscattering and outward normal vector directions and between the backscattering and grazing directions. On one hand, the backscattering peaks are insensitive to the incidence angle: they are slightly smaller for the largest angle of incidence. On the other hand, the polarization surges reveal a clear dependence on the incidence angle.

For the perpendicular plane, increasing the incidence angle results in substantial positive polarization being superimposed upon the coherent backscattering surge. The surge itself becomes more pronounced with increasing incidence angle. For the parallel plane, substantial negative polarization is superimposed upon the coherent backscattering surges and the surges become shallower. The overall background angular dependences are almost linear and vary as a function of ι. In the backscattering direction, as is correct, the enhancement factors and the absolute values of polarization are identical within each of the three sets for a given ι.

In figure 7, the intensity and polarization surges are plotted for semi-infinite media with high single-scattering albedos of 0.95, 0.99, 0.999 and 0.9999 (A-II). With increasing albedo, the polarization surges neutralize. These dependences are to be compared with the polarization curve in [25]. Several days of CPU time on a desktop workstation were needed to trace 10^5 rays for $\tilde{\omega} = 0.9999$.

The enhancement factors and minimum polarizations for $k\ell = 300$ are shown in figure 8 together with the reference numbers for plane-parallel media of conservative Rayleigh scatterers (1.5368 and -2.765% [25]). The angular scheme is A-II for the semi-infinite media with albedos 0.95, 0.99, 0.999 and 0.9999, and A-I for the rest of the cases.

The enhancement factors first increase rapidly with increasing single-scattering albedo, finally balancing out for plane albedos of about 0.5 corresponding to single-scattering albedos

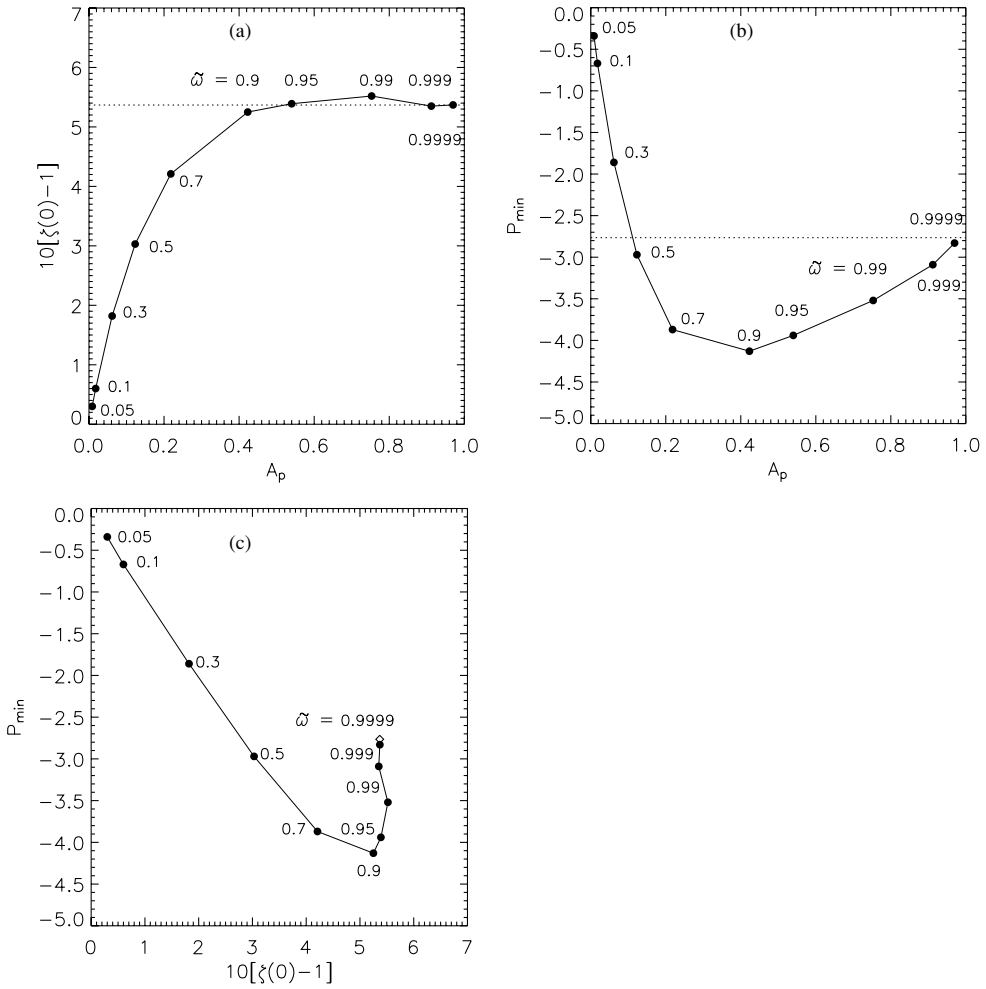

Figure 8. Enhancement factors in the backscattering direction ($\zeta(0)$) and minimum polarizations ($P_{\min}$) for semi-infinite plane-parallel media with $k\ell = 300$ consisting of Rayleigh scatterers with varying single-scattering albedos $\tilde{\omega}$. Note the differing turning points for $\zeta(0)$ and $P_{\min}$ and the convergence towards the literature values [25] for the conservative medium ($\tilde{\omega} = 1.0$: $\zeta(0) = 1.5368$, $P_{\min} = -2.765\%$): (a) $10[\zeta(0) - 1]$ versus A_p, (b) $P_{\min}$ versus A_p, and (c) $P_{\min}$ versus $10[\zeta(0) - 1]$.

0.9–0.95. The minimum polarizations first decrease sharply with increasing single-scattering albedo, reaching their minima for plane albedos of about 0.4, and thereafter increasing towards the reference value of -2.765% for the conservative plane-parallel medium. The enhancement factor reaches its maximum for single-scattering albedos below 1.0. Moreover, dictated by the current theory, the enhancement factors $\zeta(0)$ coincide for random media with differing $k\ell$ but similar $\tilde{\omega}$. Note that the earlier reference results include the polarization effects of coherent backscattering only, whereas also the first-order contributions are included in the present results. In particular, figure 8(b) suggests a first-order scattering contribution near the conservative case, where the almost linear trend in the minimum polarization appears to cross over the reference line from pure coherent backscattering. The minimum polarizations are rather inert to $k\ell$, too. The plot of the minimum polarization versus the enhancement factor

Table 2. Plane albedos A_p (%), enhancement factors $\zeta(0)$ and minimum polarizations P_{min} (%) for semi-infinite plane-parallel media of spherical scatterers (refractive index m, size parameter x). Also shown are the scattering and absorption efficiencies q_s and q_a, the single-scattering albedo $\tilde{\omega}$, the extinction mean free path $k\ell$, the polarization norm N_{12}, and the asymmetry parameters g_{11} and g_{12} (e.g., 4.20(−2) stands for 4.20×10^{-2}). The volume density of the scatterers is $v = 0.01$. For the first four entries, $x = 1.4$, $\mathrm{Re}(m) = 1.2$ and $\mathrm{Im}(m) = 10^{-v}$. For the four remaining entries, $m = 2.0 + \mathrm{i}2.0$.

	q_s	q_a	$\tilde{\omega}$	$k\ell$	N_{12}	g_{11}	g_{12}	A_p	$\zeta(0)$	P_{min}
v										
1	0.104	0.368	0.220	396	0.45	0.38	8.0(−2)	1.9	1.29	−3.2
2	0.953	4.10(−2)	0.699	1370	0.46	0.36	7.6(−2)	14	1.64	−5.9
3	0.965	4.15(−3)	0.959	1850	0.46	0.36	7.6(−2)	49	1.67	−5.2
4	0.966	4.15(−4)	0.996	1920	0.46	0.36	7.6(−2)	79	1.60	−3.4
x										
0.3	0.224	0.498	4.30(−2)	76.9	0.50	9.4(−3)	2.9(−3)	0.73	1.03	−0.3
1	1.57	1.74	0.474	40.2	0.45	0.12	3.1(−2)	9.7	1.35	−3.2
3	1.73	1.22	0.586	136	0.18	0.63	0.13	5.4	1.55	−1.6
10	1.61	0.895	0.643	532	0.20	0.73	0.13	5.9	1.55	−1.8

in figure 8(c) consists of two roughly linear branches: first, ζ and P_{min} are amplified up until $\tilde{\omega} = 0.7$–0.9, whereafter ζ is almost saturated and P_{min} is neutralized.

Table 1 gives the plane albedos A_p, enhancement factors $\zeta(0)$ and minimum polarizations P_{min} for plane-parallel media of given optical thickness τ_h consisting of Rayleigh scatterers with single-scattering albedo $\tilde{\omega}$ in the case of normal incidence. The extinction mean free path is $k\ell = 300$. For plane-parallel media of finite optical thicknesses $\tau_h = 2$ or $\tau_h = 5$ and small single-scattering albedos, the results coincide with those for semi-infinite media, but clear differences are seen for $\tilde{\omega} \geqslant 0.7$: for the larger optical thickness, the polarization surges are shallower, and the backscattering peaks are sharper. For example, maximum enhancement factors result for $\tau_h = 5$, that is, not for the smallest or the largest optical thickness. Also, the most pronounced polarization minima follow for $\tau_h = 2$ and $\tilde{\omega} = 0.99$; for $\tau_h = 5$ and semi-infinite media, the extrema are reached for $\tilde{\omega} = 0.9$. Finally, the relevant enhancement factors of table 1 are in agreement with those in [40].

3.2. Scattering beyond the Rayleigh regime

Coherent backscattering by plane-parallel media of spherical scatterers is illustrated using two examples for particle volume density of $v = 0.01$. On one hand, gradually mimicking latex particles in water, computations are carried out for a medium of absorbing spherical particles with the size parameter $x = 1.4$ and refractive index $m = 1.2 + \mathrm{i}10^{-1}$, $1.2 + \mathrm{i}10^{-2}$, $1.2 + \mathrm{i}10^{-3}$, and $1.2 + \mathrm{i}10^{-4}$ (cf [40]). 5×10^4 and 10^4 rays were traced for the first and last two cases, respectively. On the other hand, computations are carried out for a medium of absorbing spherical particles in vacuum with $x = 0.3$, 1.0, 3.0 and 10.0, and $m = 2.0 + \mathrm{i}2.0$ (10^5 rays). Table 2 (A-II) shows single-scattering characteristics for the spherical particles under consideration. All of the particles are predominantly forward scattering with $g_{11} > 0$, net positively polarizing with $N_{12} > 0$, and their polarization asymmetry parameters are positive, $g_{12} > 0$.

Figure 9 shows the reflection matrices for the latex-mimicking particles. Note the sharpening of the enhancement factor and the polarization surge with decreasing imaginary part of the refractive index (figure 9(a)). As for Rayleigh scatterers but in a more pronounced

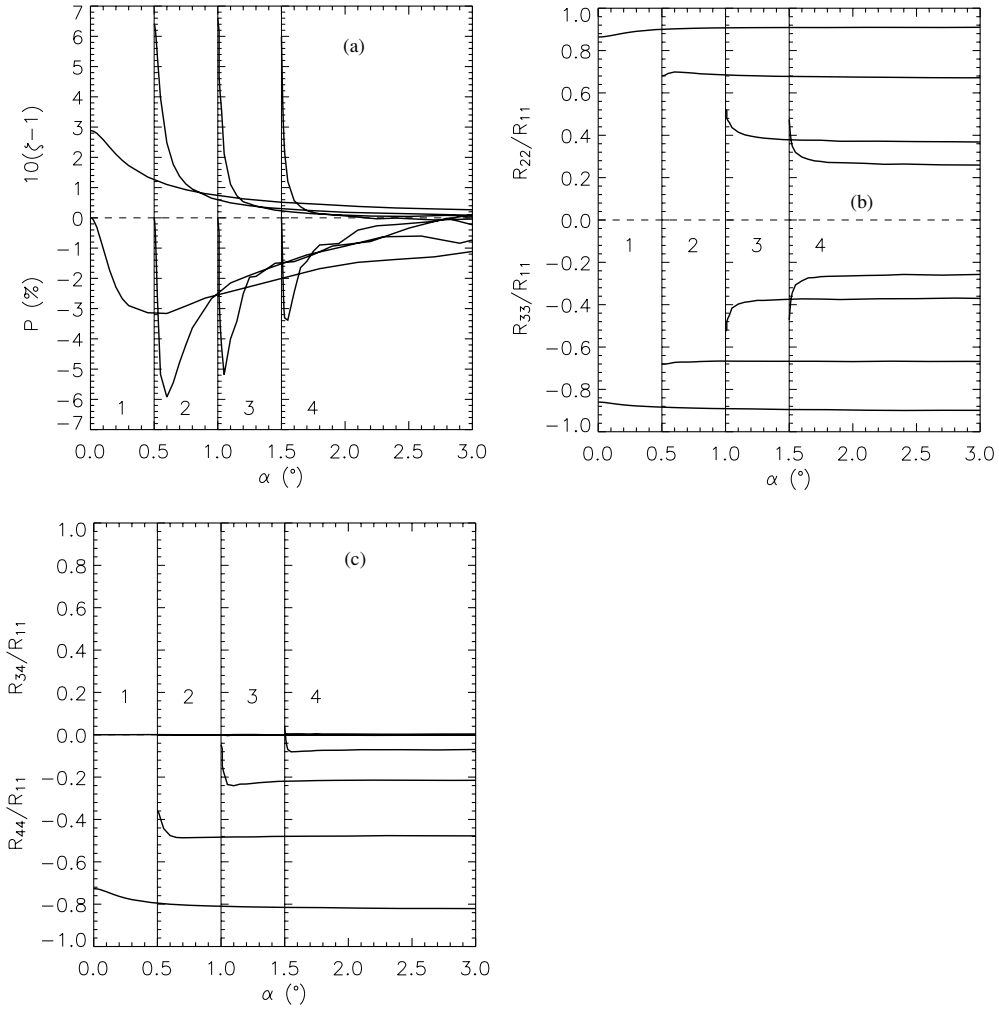

Figure 9. Reflection matrix elements for semi-infinite plane-parallel media of spherical scatterers with size parameter $x = 1.4$, real part of the refractive index $\mathrm{Re}(m) = 1.2$, varying imaginary part of the refractive index $\mathrm{Im}(m) = 10^{-1}, 10^{-2}, 10^{-3}, 10^{-4}$, and medium volume density $v = 0.01$: (a) $R_{11}/R_{11}^{\mathrm{RT}}(0)$ and $-R_{21}/R_{11}$, (b) R_{22}/R_{11} and R_{33}/R_{11}, (c) R_{34}/R_{11} and R_{44}/R_{11}.

way, the largest enhancement factors and steepest polarizations are seen for intermediate single-scattering albedos. The enhancement factor of $\zeta(0) = 1.60$ for $x = 1.4$ and $m = 1.2 + \mathrm{i}10^{-4}$ is already close to the literature value of $\zeta(0) = 1.59$ for $m = 1.2$ [40].

The element ratios R_{22}/R_{11} and R_{33}/R_{11} are, again, almost mirror images of one another, revealing a very narrow surge next to the backscattering direction (figure 9(b)). The element ratio R_{44}/R_{11} signals the conservation of the circular polarization state for the case with the smallest absorption (cf [4, 55]). The element R_{34}/R_{11} vanishes within the computational noise.

Figure 10 shows the full reflection matrices for the particles with $m = 2.0 + \mathrm{i}2.0$. The enhancement factor and polarization surge are gradually strengthened with increasing size parameter, here implying increasing single-scattering albedo (figure 10(a)). In contrast to the latex-mimicking particles above, the rest of the reflection matrix elements show little or no

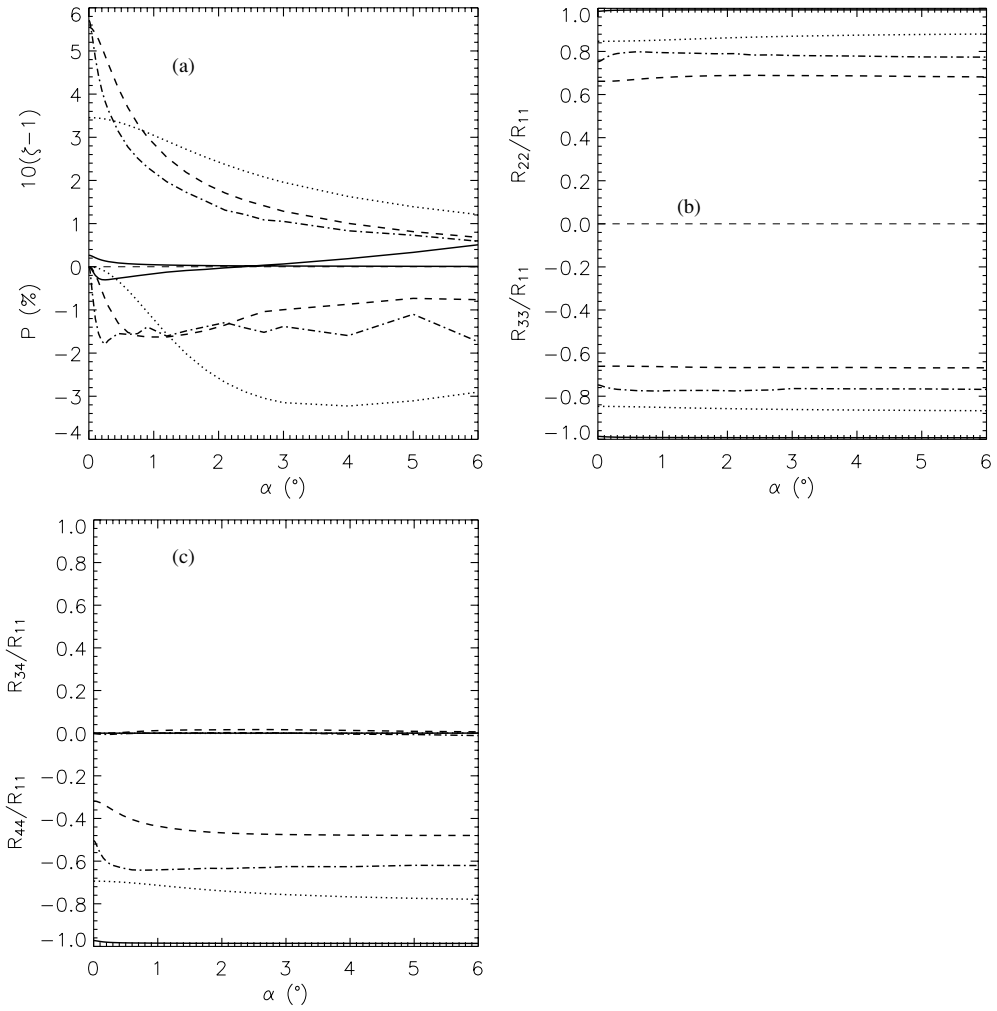

Figure 10. As in figure 9 for spherical scatterers with varying size parameter $x = 0.3$, 1, 3, 10, refractive index $m = 2.0 + \mathrm{i}2.0$, and medium volume density $v = 0.01$.

deviations from a linear dependence (figures 10(b), (c)). For the medium with the largest particles, R_{44}/R_{11} is neutralized close to the backscattering direction.

For curiousity, careful inspection of figures 9(a) and 10(a) leads to the conclusion that the angular dependence of the enhancement factor is a plausible discriminator among the eight cases under study. The discrimination becomes clear, when the polarization surges and remaining reflection matrix elements are incorporated. It is necessary to emphasize that such discrimination may generally not be possible based on backscattering characteristics only. As compared to the results for Rayleigh scatterers, the larger scatterers allow more pronounced enhancement factors ($\zeta(0) \geqslant 1.6$) and negative polarization surges ($P_{\min} \leqslant -5.8\%$).

4. Conclusions

A novel numerical Monte Carlo technique is presented for coherent backscattering by complex random media of spherical scatterers. The MC technique allows the computation of full

angular characteristics of the 4×4 reflection matrices interrelating the Stokes parameters of the incoming and outgoing radiation. The MC technique is turning useful in the interpretation of backscattering characteristics of planetary-system objects (cf [11, 56]).

Using the current MC technique in resemblance to the past radiative transfer techniques (cf [57, 58]), coherent backscattering effects can be studied for complex random media with random rough surfaces. It is possible to study such effects for media constrained by a spherical envelope with a given radial optical thickness. The effects can further be studied for discrete scatterers embedded in an optically homogeneous and isotropic medium and for random rough interfaces between two homogeneous and isotropic media (cf [59]). The MC technique allows the study of potential corrections to radiative transfer in the case of close-packed random media of scatterers.

For plane-parallel media composed of Rayleigh scatterers, the angular characteristics of the full reflection matrices have been computed for several mean free paths over the entire range of single-scattering albedos. Agreement has been reached with reference enhancement factors and polarization surges available in the literature. It has been shown that absorbing Rayleigh scatterers can yield more pronounced enhancement factors and polarization surges than non-absorbing Rayleigh scatterers. The future computations can be optimized with respect to single-scattering albedo and mean free path: first, the multiple scattering contributions from various orders of scattering for conservative media can be readily utilized to compute multiple scattering for arbitrary single-scattering albedos (less than unity) and, second, numerous mean free paths can be treated simultaneously.

For plane-parallel media of spherical scatterers beyond the Rayleigh regime, the computations show convergence towards reference enhancement factors for non-absorbing latex spheres in water and, for the first time, give the full angular dependences close to the backscattering direction. For media composed of highly absorbing scatterers, the first results indicate a resonant dependence of the polarization surge on the size of the scatterers: for spherical scatterers with volume density 1% and refractive index 2.0 + i2.0, substantial widening of the polarization surge is observed for size parameter $x = 1$, as compared to smaller or larger scatterers. An extensive study across the size parameter and refractive index domain is to be carried out in future, with special attention to be paid to the polarization states of the reverse waves.

Several challenges remain in the theory of coherent backscattering and the computational techniques for obtaining numerical results. First, it is of priority to compare the multiple scattering computations to the predictions of the electromagnetic scattering theory for constrained media of scatterers. The MC technique utilizes far-field scattering only so mean-free paths of the order of the wavelength must be treated with caution. Second, the law of energy conservation is violated for plane-parallel media of finite optical thickness, where the reflected and transmitted energy due to radiative transfer already adds up to unity. Third, the generalization of the numerical technique for nonspherical single scatterers is possible but requires vast computer programming efforts in both single and multiple scattering.

Acknowledgments

I am grateful to J I Peltoniemi, K Lumme, K Saarinen, G Videen, Yu G Shkuratov and M I Mishchenko for enlightening discussions in the course of the present study. The anonymous referees provided helpful constructive criticism. I am grateful to the Astronomical

Observatory of Torino for the enjoyable sabbatical stay. The research has been supported by the Academy of Finland.

References

[1] Shkuratov Yu G 1988 Diffractional model of the brightness surge of complex structures *Kin. Phys. Neb. Tel.* **4** 60–6
[2] Muinonen K 1989 Electromagnetic scattering by two interacting dipoles *Proc. 1989 URSI Electromagnetic Theory Symp.* (Stockholm) pp 428–30
[3] Muinonen K 1990 Light scattering by inhomogeneous media: backward enhancement and reversal of polarization *PhD Thesis* University of Helsinki
[4] Hapke B 1990 Coherent backscatter and the radar characteristics of outer planet satellites *Icarus* **88** 407–17
[5] Mishchenko M I and Dlugach J M 1993 Coherent backscatter and the opposition effect for E-type asteroids *Planet. Space Sci.* **41** 173–81
[6] Shkuratov Yu G 1989 A new mechanism of the negative polarization of light scattered by the surfaces of atmosphereless celestial bodies *Astron. Vestnik* **23** 176–80
[7] Mishchenko M I 1993 On the nature of the polarization opposition effect exhibited by Saturn's rings *Astrophys. J.* **411** 351–61
[8] Lyot B 1929 Recherches sur la polarisation de la lumière des planètes et de quelques substances terrestres *Ann. Obs. Paris* **8** 1–161
[9] von Seeliger H 1887 Zur Theorie der Beleuchtung der grossen Planeten, insbesondere des Saturn *Abh. Bayer. Akad. Wiss. Math. Naturwiss.* **Kl 16** 405–516
[10] Müller G 1893 Helligkeitsbestimmungen der grossen Planeten und einiger Asteroiden *Publ. Astrophys. Obs. Potsdam Nr. 30* **8** 193–389
[11] Muinonen K, Piironen J, Shkuratov Yu G, Ovcharenko A and Clark B 2002 Asteroid photometric and polarimetric phase effects *Asteroids III* ed W Bottke, R P Binzel, A Cellino and P Paolicchi (Tucson: University of Arizona Press) pp 123–38
[12] Muinonen K, Videen G, Zubko E and Shkuratov Yu G 2002 Numerical techniques for backscattering by random media *Optics of Cosmic Dust* (*NATO Science Series, II. Mathematics, Physics and Chemistry vol 79*) ed G Videen and M Kocifaj (Dordrecht: Kluwer) pp 261–82
[13] Muinonen K 1994 Coherent backscattering by solar system dust particles *Asteroids, Comets and Meteors 1993* ed A Milani, M Di Martino and A Cellino (Dordrecht: Kluwer) pp 271–96
[14] Shkuratov Yu G, Muinonen K, Bowell E, Lumme K, Peltoniemi J I, Kreslavsky M A, Stankevich D G, Tishkovets V P, Opanasenko N V and Melkumova L Y 1994 A critical review of theoretical models for the negative polarization of light scattered by atmosphereless solar system bodies *Earth, Moon, Planets* **65** 201–46
[15] Rosenbush V, Kiselev N, Avramchuk V and Mishchenko M 2002 Photometric and polarimetric opposition phenomena exhibited by solar system bodies *Optics of Cosmic Dust* (*NATO Science Series, II. Mathematics, Physics and Chemistry vol 79*) ed G Videen and M Kocifaj (Dordrecht: Kluwer) pp 191–224
[16] Mishchenko M, Tishkovets V and Litvinov P 2002 Exact results of the vector theory of coherent backscattering from discrete random media: an overview *Optics of Cosmic Dust* (*NATO Science Series, II. Mathematics, Physics and Chemistry vol 79*) ed G Videen and M Kocifaj (Dordrecht: Kluwer) pp 239–60
[17] Kuga Y and Ishimaru A 1984 Retroreflectance from a dense distribution of spherical particles *J. Opt. Soc. Am.* A **1** 831–5
[18] van Albada M P and Lagendijk A 1985 Observation of weak localization of light in a random medium *Phys. Rev. Lett.* **55** 2692–5
[19] Wolf P-E and Maret G 1985 Weak localization and coherent backscattering of photons in disordered media *Phys. Rev. Lett.* **55** 2696–9
[20] Watson K M 1969 Multiple scattering of electromagnetic waves in an underdense plasma *J. Math. Phys.* **10** 688–702
[21] de Wolf D A 1971 Electromagnetic reflections from an extended turbulent medium: cumulative forward-scatter single backscatter approximation *IEEE Trans. Antennas Propag.* **19** 254–62
[22] van Albada M P, van der Mark M B and Lagendijk A 1988 Polarisation effects in weak localisation of light *J. Phys. D: Appl. Phys.* **21** S28–31
[23] Ozrin V D 1992 Exact solution for coherent backscattering of polarized light from a random medium of Rayleigh scatterers *Waves Random Media* **2** 141–64

[24] Amic E, Luck J-M and Nieuwenhuizen Th M 1997 Multiple Rayleigh scattering of electromagnetic waves *J. Phys. I* **7** 445–83
[25] Mishchenko M I, Luck J-M and Nieuwenhuizen Th M 2000 Full angular profile of the coherent polarization opposition effect *J. Opt. Soc. Am.* A **17** 888–91
[26] Ismagilov F M and Kravtsov Yu A 1993 Backscattering polarization effects on a system of two randomly oriented scatterers *Waves Random Media* **3** 17–24
[27] Mishchenko M I 1996 Coherent backscattering by two-sphere clusters *Opt. Lett.* **21** 623–5
[28] Muinonen K and Lumme K 1991 Light scattering by solar system dust: the opposition effect and the reversal of linear polarization *IAU Colloquium 126, Origin and Evolution of Dust in the Solar System* (Dordrecht: Kluwer) pp 159–62
[29] Lindell I V, Sihvola A H, Muinonen K and Barber P W 1991 Scattering by a small object close to an interface: I. Exact image theory formulation *J. Opt. Soc. Am.* A **8** 472–6
[30] Muinonen K, Sihvola A H, Lindell I V and Lumme K 1991 Scattering by a small object close to an interface: II. Study of backscattering *J. Opt. Soc. Am.* A **8** 477–82
[31] Ismagilov F M 1995 Polarization effects in backscattering by a particle near the interface *Waves Random Media* **5** 27–32
[32] Lumme K, Green K, Muinonen K and Penttilä A 2003 Light scattering by large densely-packed aggregates: a wave-optical approach *Electromagnetic and Light Scattering—Theory, Measurements, and Applications VII* (*Bremen, Germany, 8–12 Sept. 2003*) pp 220–3
[33] Muinonen K 2003 Light scattering by tetrahedral particles in the Kirchhoff approximation *Electromagnetic and Light Scattering—Theory, Measurements, and Applications VII* (*Bremen, Germany, 8–12 Sept. 2003*) pp 251–4
[34] Akkermans E, Wolf P E and Maynard R 1986 Coherent backscattering of light by disordered media: analysis of the peak line shape *Phys. Rev. Lett.* **56** 1471–4
[35] Stephen M J and Cwilich G 1986 Rayleigh scattering and weak localization: effects of polarization *Phys. Rev.* B **34** 7564–72
[36] Iwai T, Furukawa H and Asakura T 1995 Numerical analysis of enhanced backscatterings of light based on Rayleigh-Debye scattering theory *Opt. Rev.* **2** 413–19
[37] Ishii K, Iwai T, Uozumi J and Asakura T 1998 Optical free-path-length distribution in a fractal aggregate and its effect on enhanced backscattering *Appl. Opt.* **37** 5014–8
[38] Saxon D S 1955 Tensor scattering matrix for the electromagnetic field *Phys. Rev.* **100** 1771–5
[39] Bohren C F and Huffman D R 1983 *Absorption and Scattering of Light by Small Particles* (New York: Wiley)
[40] Mishchenko M I 1992 Enhanced backscattering of polarized light from discrete random media: calculations in exactly the backscattering direction *J. Opt. Soc. Am.* A **9** 978–82
[41] van Tiggelen B and Skipetrov S 2002 *Wave Scattering in Complex Media: From Theory to Applications* (Dordrecht: Kluwer)
[42] Sebbah P 2001 *Waves and Imaging through Complex Media* (Dordrecht: Kluwer)
[43] Van Rossum M C W and Nieuwenhuizen Th M 1999 Multiple scattering of classical waves: microscopy, mesoscopy, and diffusion *Rev. Mod. Phys.* c **71** 313–71
[44] Fouque J-P 1999 *Diffuse Waves in Complex Media* (Dordrecht: Kluwer)
[45] Barabanenkov Yu N, Kravtsov Yu N, Ozrin V D and Saichev A I 1991 Enhanced backscattering in optics *Progress in Optics* vol 29 ed E Wolf (Amsterdam: Elsevier) pp 65–197
[46] Tsang L, Kong J A and Shin R T 1985 *Theory of Microwave Remote Sensing* (New York: Wiley)
[47] Barabanenkov Yu N 1973 Wave corrections to the transfer equation for backscattering *Izv. Vyssch. Uchebn. Zaved. Radiofiz.* **16** 88–96
[48] Muinonen K 2002 Coherent backscattering by absorbing and scattering media *Electromagnetic and Light Scattering by Non-spherical Particles, Gainesville 2002* ed B Gustafson, L Kolokolova and G Videen (Adelphi: Army Research Laboratory) pp 223–6
[49] Tishkovets V P, Litvinov P V and Lyubchenko M V 2002 Coherent opposition effects for semi-infinite discrete random medium in the double-scattering approximation *J. Quant. Spectrosc. Radiat. Transfer* **72** 803–11
[50] Hansen J E and Travis L D 1974 Light scattering in planetary atmospheres *Space Sci. Rev.* **16** 527–610
[51] Muinonen K 2000 Light scattering by stochastically shaped particles *Light Scattering by Nonspherical Particles: Theory, Measurements, and Applications* ed M I Mishchenko, J W Hovenier and L D Travis (San Diego, CA: Academic) pp 323–52
[52] Danby J M A 1992 *Fundamentals of Celestial Mechanics* (Richmond: Willmann-Bell)
[53] Coulson K L, Dave J V and Sekera Z 1960 *Tables Related to Radiation Emerging from a Planetary Atmosphere with Rayleigh Scattering* (Berkeley and Los Angeles: University of California Press)

[54] Press W H, Teukolsky S A, Vetterling W T and Flannery B P 1992 *Numerical Recipes in Fortran, The Art of Scientific Computing* 2nd edn (Cambridge: Cambridge University Press)
[55] Ostro S J 1993 Planetary radar astronomy *Rev. Mod. Phys.* **65** 1235–73
[56] Boehnhardt H, Bagnulo S, Muinonen K, Barucci M A, Kolokolova L, Dotto E and Tozzi G P 2004 Surface characterization of 28978 Ixion (2001 KX_{76}) *Astron. Astrophys. Lett.* **415** L21–5
[57] Lumme K, Peltoniemi J I and Irvine W M 1990 Diffuse reflection in stochastically bounded semi-infinite media *Trans. Theory Stat. Phys.* **19** 317–32
[58] Peltoniemi J I 1993 Radiative transfer in stochastically inhomogeneous media *J. Quant. Spectrosc. Radiat. Transfer* **50** 655–71
[59] Videen G, Muinonen K and Lumme K 2003 Coherence, power laws, and the negative polarization surge *Appl. Opt.* **42** 3647–52